Aeroelastic Trim Drag Optimization of Mach 0.8 Transonic Truss-Braced Wing Aircraft using High-Lift Devices and Control Surfaces

Juntao Xiong*
KBR Wyle, Inc., Moffett Field, CA 94035
Nhan Nguyen†
NASA Ames Research Center, Moffett Field, CA 94035
Robert E. Bartels‡
NASA Langley Research Center, Hampton, VA 23681

This paper presents an aeroelastic trim drag optimization study of the Mach 0.8 Transonic Truss-Braced Wing (TTBW) aircraft using the High-lift devices and control surfaces. An aero-structural analysis solver VSPAERO with transonic small disturbance, integral boundary-layer, and wing-strut interference corrections coupled to mode shapes computed by NASTRAN using the Galerkin method is developed to provide a rapid aircraft aeroelastic performance evaluation. Three different flight conditions corresponding to Mach 0.8 are selected for the aeroelastic trim drag optimization at the design and off-design cruise lift coefficients. The preliminary optimization results show that the TTBW aircraft with the optimized deflection of the high-lift devices and control surfaces achieves a drag reduction of about 8.2 counts, 6.5 counts, and 9.7 counts corresponding to the lift coefficients 0.661, 0.695, and 0.729, respectively. A high-fidelity CFD solver FUN3D is used to verify the aeroelastic trim drag optimization.

I. Introduction

The aircraft industry has been responding to the need for more energy-efficient aircraft by redesigning airframes to be aerodynamically and structurally more efficient. The Mach 0.8 Transonic Truss-Braced Wing (TTBW)[1,2,3,4] aircraft shown in Figure 1 is designed to be aerodynamically efficient by employing an aspect ratio of about 19.55, which is significantly greater than those of conventional aircraft cantilever wings. The main idea is to use truss structures to alleviate the wing root bending moment, so that a significant increase in the wing aspect ratio could be afforded. The design of a truss-braced wing is a Multidisciplinary Design Analysis and Optimization (MDAO) process that strives to achieve a delicate balance between aerodynamic and structural efficiencies. Another option for managing the aeroelastic behavior of the aircraft is through control system design. The control system could be made to both suppress undesirable motion and shape the flexible structure in pursuit of improved performance goals.

*Aerospace Engineer, Intelligent System Division, juntao.xiong@nasa.gov, AIAA Member
†Senior Research Scientist and Technical Group Lead, Intelligent Systems Division, nhan.t.nguyen@nasa.gov, Associate Fellow AIAA
‡Research Aerospace Engineer, NASA Langley Research Center, MS 340, robert.e.bartels@nasa.gov, AIAA Senior Member

Figure 1 Boeing SUGAR Mach 0.8 Transonic Truss-Braced Wing (TTBW) Aircraft Concept

The concept of variable-camber continuous trailing-edge flap (VCCTEF) concept developed by NASA was proposed by Nguyen in 2010.[5,6] The use of VCCTEF for the active control of a aeroelastic wing such as suppressing flutter, stabilizing the vehicle response to gusts, and reducing drag have been studied.[7,8,9,10] Nguyen et al.[11] conducted aerodynamic optimization for the Mach 0.8 TTBW aircraft 1g shape with the VCCTEF. The study indicates the VCCTEF system offers potential payoff in drag reduction by actively controlling the shape of the wing for the Mach 0.8 TTBW aircraft. However, additional actuators are needed to drive the VCCTEF, which will introduce a weight penalty that could reduce the benefit of drag reduction. Airbus investigated adaptive drooped hinged flap (ADHF) which utlizes the high-lift system for in-flight aerodynamic optimization.[12] The optimized high-lift system provides the maximum aerodynamic efficiency for low approach speeds and low take off drag, while overall system small and simple to provide low weight and low complexity. It open up a probability to utilize the high-lift device and control surface for the aerodynamic efficiency improvement at cruise condition. In this paper, an aeroelastic trim drag optimization study of Mach 0.8 TTBW aircraft using the high-lift systems and control surfaces is conducted. Three different flight conditions corresponding to Mach 0.8 are selected for the aeroelastic trim drag optimization at the design and off-design cruise lift coefficients. A high-fidelity CFD solver FUN3D is used to verify the optimization results in the end.

II. Aero-Structural Model of the Transonic Truss-Braced Wing

A. VSPAERO Model

In order to develop a rapid aeroelastic analysis that facilitates a vehicle MDAO process, a lower-fidelity aerodynamic model of the TTBW is necessary. VSPAERO[13] is a solver that includes both the vortex lattice method and the full panel method based on generalized vortex rings. The core VSPAERO solver is based on an agglomerated multi-pole approach, coupled with a preconditioned linear solver, to reduce solution times. Adaptive wakes, time-accurate, unsteady analyses, and propeller modeling are all supported. The VSPAERO based tool has been implemented with a 2D transonic and viscous flow corrections via the TSD/IBL method and transonic wing-strut interference correction for the Mach 0.8 TTBW aircraft simulation.[14]

The VSPAERO model is used for the aerodynamic analysis of the cruise 1g shape TTBW geometry for the Mach 0.8 TTBW aircraft configuration. Wind tunnel test data of the cruise shape geometry in NASA Ames 11-Ft Transonic Wind Tunnel are available for validation of the VSPAERO models. Figure 2 shows the plots of the lift and drag coefficients computed by VSPAERO and FUN3D[14] for Mach 0.8 and a Reynolds number of 2.17 million. The computed results are compared to Run 378 wind tunnel data. The lift coefficients are somewhat overpredicted for VSPAERO and FUN3D simulations. With all the corrections applied to the VSPAERO model for transonic viscous flow and wing-strut interference aerodynamics, the lift and drag coefficients match well to the wind tunnel data and FUN3D simulations, although there is a small discrepancy in the drag polar at lower lift coefficients. The VSPAERO+TSD/IBL with the

wing-strut interference correction model can be used as a fast and reliable tool for the TTBW aircraft conceptual analysis and design.

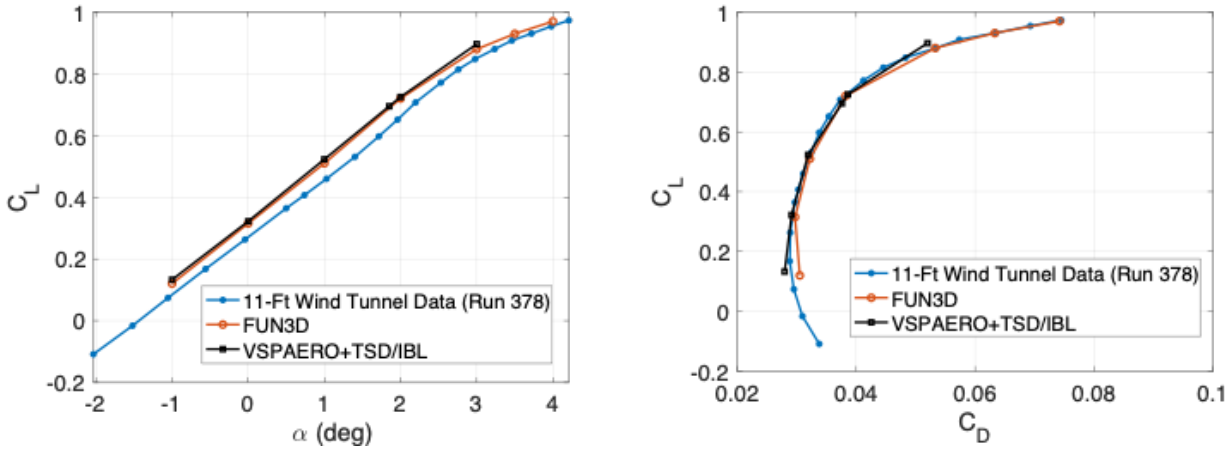

(a) Lift Curve

(b) Drag Polar

Figure 2 Mach 0.8 TTBW Lift Curve and Drag Polar at Mach 0.8 and $Re = 2.17 \times 10^6$

B.Galerkin Method

A NASTRAN finite-element model (FEM) of the Mach 0.8 TTBW is available from Boeing. The NASTRAN FEM comprises a detail structural model of the wing and struts, a shell structural model of the fuselage section that joins with the wing, and a beam-stick model of the rest of the fuselage and the tail empennage. This is shown in Figure 3. To reflect the estimated gross weights the fuel model in the Boeing NASTRAN model has been updated. The wing and strut root movements are set to zero for the cantilever wing model. The revised NASTRAN model is used to extract mode shapes for the aeroelastic analysis for the Mach 0.8 TTBW using the Galerkin method. Figure 4 shows the mode shapes of the first six modes.

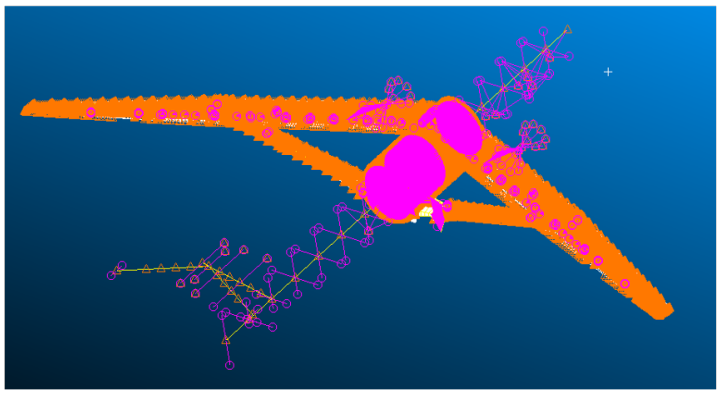

Figure 3 Boeing Mach 0.8 NASTRAN Finite-Element Model

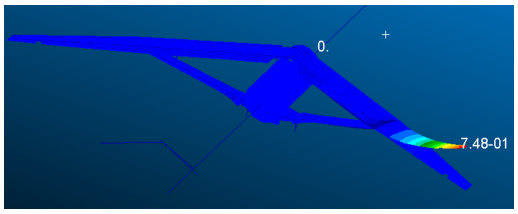

(a) 1st Mod

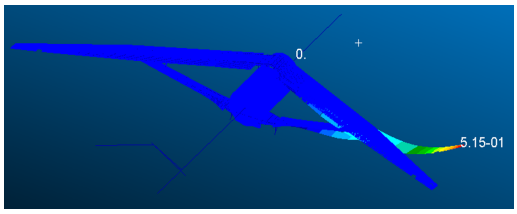

(b) 2nd Mode

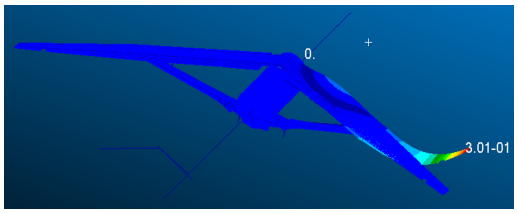

(c) 3rd Mode

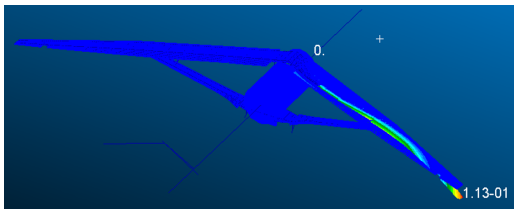

(d) 4th Mode

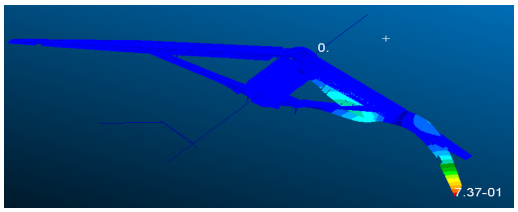

(e) 5th Mode

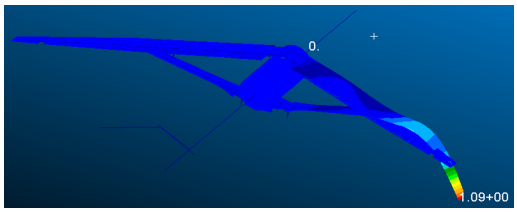

(f) 6th Mode

Figure 4 Boeing Mach 0.8 TTBW NASTRAN Mode Shapes for 50% Fuel.

The static structural equation can be written as

$$[K]U_a = F_a \tag{1}$$

where $|K|$ is the stiffness matrix, U_a is the displacement vector, and F_a is the aerodynamic force vector. If the displacements are written as an expansion in terms of natural vibration modes ϕ_i

$$U_a = \sum_{i=1}^{N_{modes}} q_i \phi_i \tag{2}$$

where q_i are the generalized displacements. Substitution of the series representation into the structural equation and premultiplying by ϕ^T, we obtain

$$\phi^T [K] \phi q = \phi^T F_a \tag{3}$$

where $\phi^T [K] \phi$ is the diagonal generalized stiffness matrix and $\phi^T F_a$ is the generalized aerodynamic force vector. After the generalized displacements q are calculated from the decoupled equations, the structural deformation due to aerodynamic force U_a can be obtained from Eq (2). The structural deformation due to the aircraft weight U_w is obtained from SOL 101 NASTRAN solution. Figure 5 shows the geometry deformation of the Mach 0.8 TTBW with 50% fuel under gravity load. The overall structural deformation can be calculated by

$$U = U_a + U_w \tag{4}$$

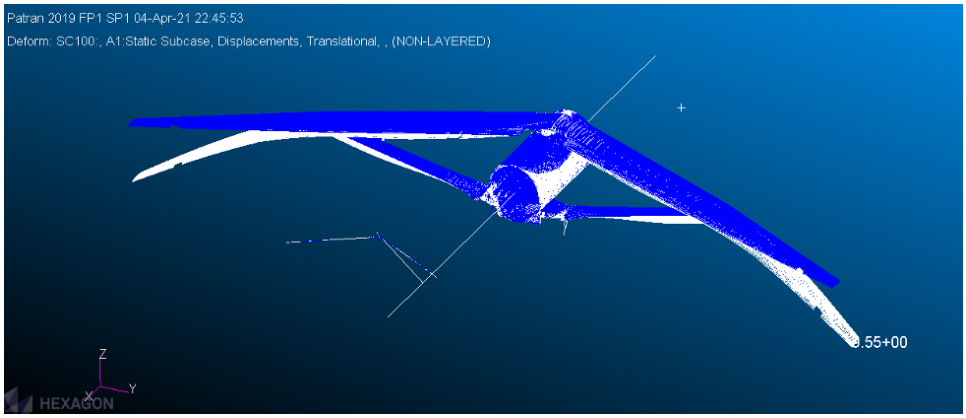

Figure 5 Mach 0.8 TTBW Structural Deformation Due to Gravity Load 50% Fuel.

C. Static Aeroelastic Analysis

A basic schematic of the aeroelastic modeling strategy is depicted by Fig. 6. The VSPAERO model is couple to the mode shapes computed by NASTRAN using the Galerkin method to provide a rapid aero-structural analysis. At each iteration of the aeroelastic simulation the aerodynamic force F_z and moments M_x and M_y converted from wing sectional lift and pitching moment are applied to the Galerkin method.

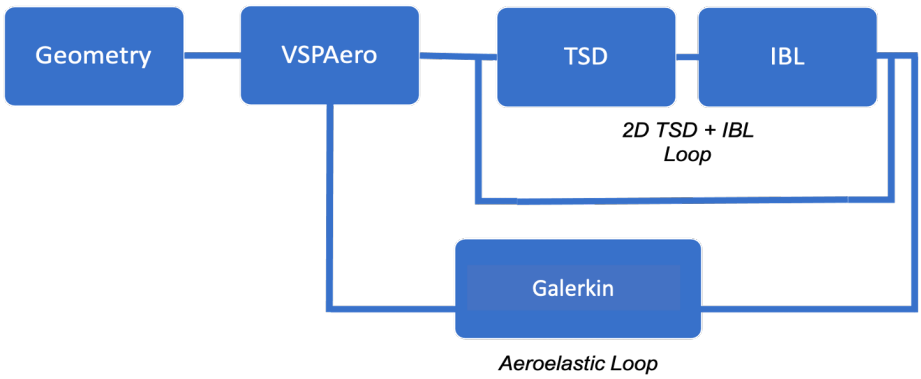

Figure 6 VSPAERO Aeroelastic Simulation Scheme Flow Chart

The wing coordinate system is shown in the following Fig. 7.

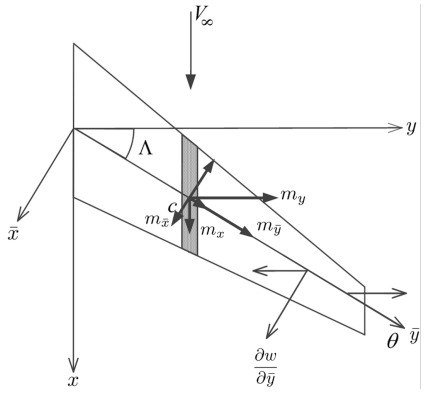

Figure 7 Wing Coordinate System

The distributed force and moments in the elastic axis coordinate system $(\bar{x}, \bar{y}, z)$ due to aerodynamics are given by

$$f_z = c_l q_\infty c \cos\Lambda \tag{5}$$

$$m_{\bar{x}} = \left[\left(c_{m_{ac}} + c_{m_x} \tan\Lambda\right) q_\infty c^2 + c_l q_\infty c e\right] \cos\Lambda \sin\Lambda \tag{6}$$

$$m_{\bar{y}} = \left[\left(c_{m_{ac}} + c_{m_x} \tan\Lambda\right) q_\infty c^2 + c_l q_\infty c e\right] \cos^2\Lambda \tag{7}$$

The hermite cubic interpolation function for the beam element in the finite-element method is

$$\mathbf{N}_w^{(i)^\top}(\bar{y}_i) = \begin{bmatrix} 1 - 3\left(\frac{\bar{y}_i}{l_i}\right)^2 + 2\left(\frac{\bar{y}_i}{l_i}\right)^3 \\ l_i\left[\frac{\bar{y}_i}{l_i} - 2\left(\frac{\bar{y}_i}{l_i}\right)^2 + \left(\frac{\bar{y}_i}{l_i}\right)^3\right] \\ 3\left(\frac{\bar{y}_i}{l_i}\right)^2 - 2\left(\frac{\bar{y}_i}{l_i}\right)^3 \\ l_i\left[-\left(\frac{\bar{y}_i}{l_i}\right)^2 + \left(\frac{\bar{y}_i}{l_i}\right)^3\right] \end{bmatrix} \tag{8}$$

$$\frac{d\mathbf{N}_w^{(i)^\top}(\bar{y}_i)}{d\bar{y}} = \begin{bmatrix} \frac{1}{l_i}\left[-6\left(\frac{\bar{y}_i}{l_i}\right) + 6\left(\frac{\bar{y}_i}{l_i}\right)^2\right] \\ 1 - 4\left(\frac{\bar{y}_i}{l_i}\right) + 3\left(\frac{\bar{y}_i}{l_i}\right)^2 \\ \frac{1}{l_i}\left[6\left(\frac{\bar{y}_i}{l_i}\right) - 6\left(\frac{\bar{y}_i}{l_i}\right)^2\right] \\ -2\left(\frac{\bar{y}_i}{l_i}\right) + 3\left(\frac{\bar{y}_i}{l_i}\right)^2 \end{bmatrix} \tag{9}$$

The elemental force vector due to bending in the element coordinate system $(\bar{x}, \bar{y}, z)$ is

$$\mathbf{F}_w^{(i)} = \begin{bmatrix} F_{z_1} \\ M_{\bar{x}_1} \\ F_{z_2} \\ M_{\bar{x}_2} \end{bmatrix} = \int_0^{l_i} \mathbf{N}_w^{(i)^\top}(\bar{y}_i)\left(f_z + \frac{dm_{\bar{x}}}{d\bar{y}_i}\right) d\bar{y}_i = \int_0^{l_i} \mathbf{N}_w^{(i)^\top}(\bar{y}_i)\, f_z d\bar{y}_i - \int_0^{l_i} \frac{d\mathbf{N}_w^{(i)^\top}(\bar{y}_i)}{d\bar{y}} m_{\bar{x}} d\bar{y}_i \tag{10}$$

The elemental force vector due to bending in the aircraft coordinate system (x, y, z) is

$$\mathbf{F}_w^{(i)} = \begin{bmatrix} F_{z_1} \\ M_{x_1} \\ M_{y_1} \\ F_{z_2} \\ M_{x_2} \\ M_{y_2} \end{bmatrix} = \begin{bmatrix} F_{z_1} \\ M_{\bar{x}_1} \cos\Lambda \\ -M_{\bar{x}_1} \sin\Lambda \\ F_{z_2} \\ M_{\bar{x}_2} \cos\Lambda \\ -M_{\bar{x}_2} \sin\Lambda \end{bmatrix} \tag{11}$$

The linear interpolation function for the rod element in the finite-element method is

$$\mathbf{N}_\theta^{(i)^\top}(\bar{y}_i) = \begin{bmatrix} 1 - \frac{x_i}{l_i} \\ \frac{x_i}{l_i} \end{bmatrix} \tag{12}$$

The elemental force vector due to torsion in the element coordinate system $(\bar{x}, \bar{y}, z)$ is

$$\mathbf{F}_\theta^{(i)} = \begin{bmatrix} M_{\bar{y}_1} \\ M_{\bar{y}_2} \end{bmatrix} = \int_0^{l_i} \mathbf{N}_\theta^{(i)^\top}(\bar{y}_i)\, m_{\bar{y}}\, d\bar{y}_i \tag{13}$$

The elemental force vector due to torsion in the aircraft coordinate system (x, y, z) is

$$\mathbf{F}_\theta^{(i)} = \begin{bmatrix} M_{x_1} \\ M_{y_1} \\ M_{x_2} \\ M_{y_2} \end{bmatrix} = \begin{bmatrix} M_{\bar{y}_1} \sin\Lambda \\ M_{\bar{y}_1} \cos\Lambda \\ M_{\bar{y}_2} \sin\Lambda \\ M_{\bar{y}_2} \cos\Lambda \end{bmatrix} \tag{14}$$

The total element force vector in the aircraft coordinate system (x, y, z) is

$$\mathbf{F}_w^{(i)} = \begin{bmatrix} F_{z_1} \\ M_{x_1} \\ M_{y_1} \\ F_{z_2} \\ M_{x_2} \\ M_{y_2} \end{bmatrix} = \begin{bmatrix} F_{z_1} \\ M_{\bar{x}_1} \cos\Lambda + M_{\bar{y}_1} \sin\Lambda \\ -M_{\bar{x}_1} \sin\Lambda + M_{\bar{y}_1} \cos\Lambda \\ F_{z_2} \\ M_{\bar{x}_2} \cos\Lambda + M_{\bar{y}_2} \sin\Lambda \\ -M_{\bar{x}_2} \sin\Lambda + M_{\bar{y}_2} \cos\Lambda \end{bmatrix} \tag{15}$$

The nodal forces on an element is shown in the following Fig. 8

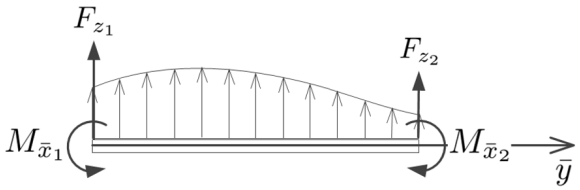

Figure 8 Wing Nodal Force Flow Chart

The Galerkin solution provides the structural deformation of the Mach 0.8 TTBW. Figure 9 shows the Mach 0.8 TTBW with 50% fuel wing bending displacement and twist at Mach 0.80, angle of attack 2°, and altitude 40,000ft. The results show a wing tip deflection 17.25 inches and twist down 1.2° at this condition.

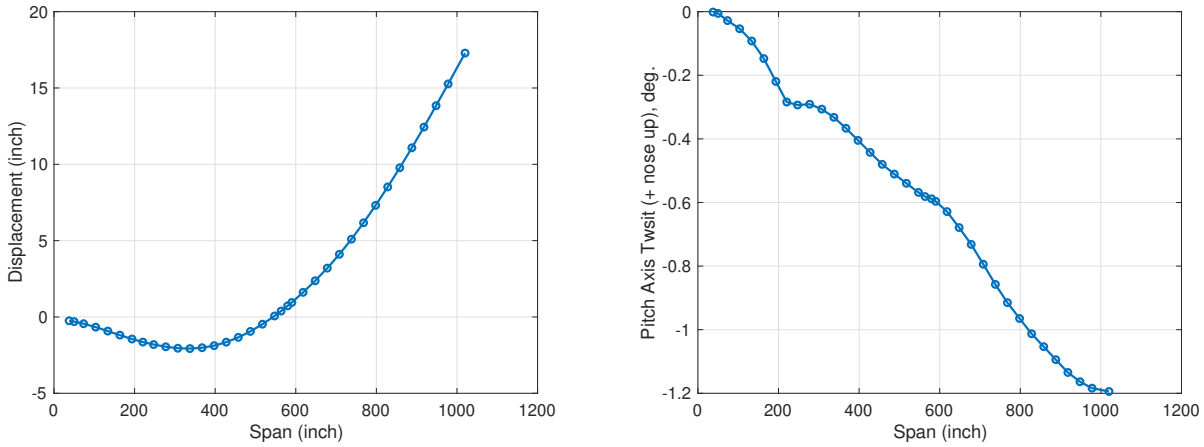

(a) Bending Deflection (b) Twist Angle

Figure 9 Mach 0.8 TTBW Wing Bending Deflection and Twist at $M_\infty = 0.8$ and $\alpha = 2°$

III. Optimization of High-Lift System with Control Surfaces

A. TTBW High-Lift System and Control Surfaces

The planform of the high-lift devices and control surfaces configuration is shown in Fig. 10. There are 13 high-lift devices and control surfaces are used for the optimization, which are listed in the Table 1. The four segments of flap and spoilers are numbered from wing root to wing tip. The two segments of aileron are also numbered from wing root to wing tip. In the optimization the spoilers are assumed to rig for for upward and downward deflections and the ailerons are assumed to rig for symmetric deflections.

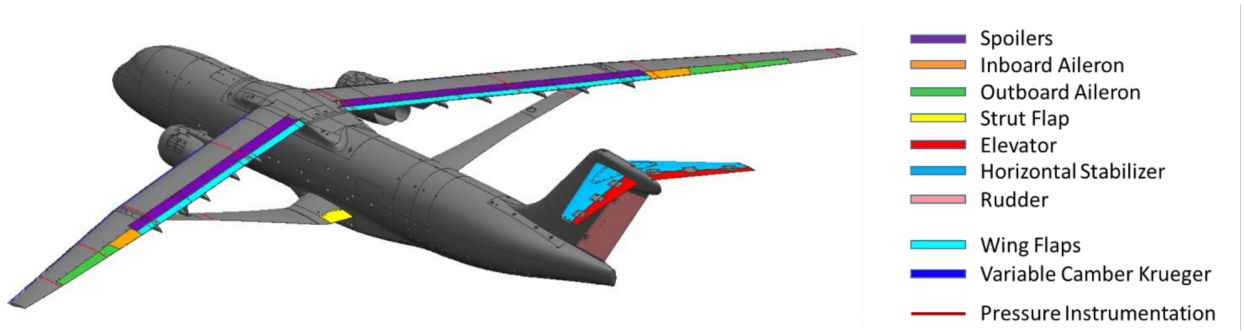

Figure 10 High-lift Devices and Control Surfaces Configuration (Credit: Harrison et al.[4])

Table 1 High-lift Device and Control Surfaces

Segment	flap-1	flap-2	flap-3	flap-4	spoiler-1	spoiler-2	spoiler-3	spoiler-4	aileron-1	aileron-2	strut flap	elevator	h-tail
Symbol	δ_1	δ_2	δ_3	δ_4	δ_5	δ_6	δ_7	δ_8	δ_9	δ_{10}	δ_{11}	δ_{12}	δ_{13}

B. Aeroelastic Trim Drag Optimization

The goal of the optimization scheme is to minimize the trim drag coefficient of the jig shape geometry for the TTBW aircraft at three different flight conditions via changing the high-lift devices and control surfaces deflections.

The cost function is defined as:

$$J(\alpha, \delta_i) = C_D + \lambda_1(C_L^* - C_L) + \lambda_2(C_m^* - C_m - \frac{Tz_e}{q_\infty S\bar{c}}) \tag{16}$$

where λ_1 and λ_2 are the adjoint variables, T is the engine thrust which is equal to the drag force, z_e is the offset of the thrust centerline from the aircraft center of gravity (CG), q_∞ is the dynamic pressure, S is the wing reference area, $\bar{c}$ is the mean aerodynamic chord (MAC), C_L^* is the trim lift coefficient and C_m^* is the zero trim pitching moment coefficient, and δ_i ($i = 1, 2, ..., 13$) represents the high-lift devices and control surfaces deflections. The lift and pitching moment constraints are added to the optimization algorithm. The pitching moment contribution by the engine thrust is included. Three trim lift coefficients $C_{L_1}^- = 0.661$, $C_{L_2}^- = 0.695$, and $C_{L_3}^- = 0.729$ are selected in the aeroelastic trim drag optimization, which correspond to the 20% fuel, 50% fuel, and 80% fuel flight conditions.

A steepest descent algorithm for updating the design variables can be represented by the following equations:

$$\alpha_{k+1} = \alpha_k - \epsilon\frac{\partial J}{\partial \alpha} \tag{17}$$

$$\delta_{h_{k+1}} = \delta_{h_k} - \epsilon\frac{\partial J}{\partial \delta_h} \tag{18}$$

Here, the design variables at iteration k are updated based on the partial derivatives of the cost function with respect to the design variables, which are calculated using a small-perturbation, second-order central difference scheme, and ϵ is a step size term.

Two optimization studies are conducted in this paper. The first optimization starts with the original jig twist optimized for wind tunnel test. The second optimization starts with flight-optimized jig twist for full-scale performance. The flight-optimized jig twist is obtained via a jig twist optimization study using 5^{th} order Chebyshev polynomials at flight condition.[15]

C. Optimization Results with Original Jig Twist

The aeroelastic trim drag optimization results using the original jig twist are presented in the Table 2 - 4. After the design the aeroelastic trim drag are reduced by 1.12%, 0.88%, and 1.51% with the high-lift devices and control surfaces at the three flight conditions.

Table 2 Aeroelastic Trim Drag Optimization Results from VSPAERO for $C_{L_1} = 0.661$

	C_L	C_D	α (deg)	ΔC_D (counts)	$\Delta C_D/C_{D_{Baseine}}$	L/D
Baseline	0.661	0.03201	1.552	-	-	20.65
Design (with original jig twist)	0.661	0.03165	1.626	3.6	1.12%	20.88

Table 3 Aeroelastic Trim Drag Optimization Results from VSPAERO for $C_{L_2} = 0.695$

	C_L	C_D	α (deg)	ΔC_D (counts)	$\Delta C_D/C_{D_{Baseline}}$	L/D
Baseline	0.695	0.03285	1.682	-	-	21.16
Design (with original jig twist)	0.695	0.03256	1.713	2.9	0.88%	21.34

Table 4 Aeroelastic Trim Drag Optimization Results from VSPAERO for $C_{L_3} = 0.729$

	C_L	C_D	α (deg)	ΔC_D (counts)	$\Delta C_D / C_{D_{Baseline}}$	L/D
Baseline	0.729	0.03502	1.832	-	-	20.82
Design (with original jig twist)	0.729	0.03449	1.893	5.3	1.51%	21.13

D. Optimization Results with Optimized Jig Twist

The aeroelastic trim drag optimization using the flight-optimized jig twist results are presented in the Table 5 - 7. In the tables the drag reduction ΔC_D refers to the baseline drag. Table 8 - 10 show the deflection angles of the high-lift device and control surfaces. With the optimized jig twist the aeroelastic trim drag are reduced by 2.63%, 1.98%, and 2.85% with the high-lift devices and control surfaces at the three flight conditions.

Table 5 Aeroelastic Trim Drag Optimization Results from VSPAERO for $C_{L_1} = 0.661$

	C_L	C_D	α (deg)	ΔC_D (counts)	$\Delta C_D / C_{D_{Baseline}}$	L/D
Jig twist optimization	0.661	0.03144	1.633	5.7	1.78%	21.02
Design (with optimized jig twist)	0.661	0.03119	1.651	8.2	2.63%	21.19

Table 6 Aeroelastic Trim Drag Optimization Results from VSPAERO for $C_{L_2} = 0.695$

	C_L	C_D	α (deg)	ΔC_D (counts)	$\Delta C_D / C_{D_{Baseline}}$	L/D
Jig twist optimization	0.695	0.03237	1.743	4.8	1.47%	21.47
Design (with optimized jig twist)	0.695	0.03220	1.792	6.5	1.98%	21.58

Table 7 Aeroelastic Trim Drag Optimization Results from VSPAERO for $C_{L_3} = 0.729$

	C_L	C_D	α (deg)	ΔC_D (counts)	$\Delta C_D / C_{D_{Baseline}}$	L/D
Jig twist optimization	0.729	0.03429	1.931	7.3	2.08%	21.26
Design (with optimized jig twist)	0.729	0.03405	1.957	9.7	2.85%	21.41

Table 8 High-lift Device and Control Surfaces Deflection Angles (deg.) for $C_{L_1} = 0.661$

	δ_1	δ_2	δ_3	δ_4	δ_5	δ_6	δ_7	δ_8	δ_9	δ_{10}	δ_{11}	δ_{12}	δ_{13}
Design	-0.39	-0.91	-1.08	-0.42	0.25	-1.05	-1.12	-0.51	-0.35	0.17	-0.78	-1.55	-0.42

Table 9 High-lift Device and Control Surfaces Deflection Angles (deg.) for $C_{L_2} = 0.695$

	δ_1	δ_2	δ_3	δ_4	δ_5	δ_6	δ_7	δ_8	δ_9	δ_{10}	δ_{11}	δ_{12}	δ_{13}
Design	-0.35	-0.65	-0.73	-0.37	0.23	-0.55	-0.66	-0.28	-0.26	0.15	-0.63	-1.52	-0.56

Table 10 High-lift Device and Control Surfaces Deflection Angles (deg.) for $C_{L_3} = 0.729$

	δ_1	δ_2	δ_3	δ_4	δ_5	δ_6	δ_7	δ_8	δ_9	δ_{10}	δ_{11}	δ_{12}	δ_{13}
Dessign	-0.35	-1.53	-2.23	-0.55	0.28	-1.49	-1.76	-0.48	-0.41	0.25	-1.23	-1.18	-0.86

D. High-fidelity CFD Simulation

To validate the aeroelastic trim drag optimization, a validation study using high-fidelity CFD solver FUN3D is performed. FUN3D[16,17] solves the unsteady three-dimensional Navier-Stokes equations on mixed-element grids using a vertices-centered finite-volume method. Information exchange for flow computation on different partitions using multiple CPUs is implemented through the MPI (Message Passing Interface) protocol. It employs an implicit upwind algorithm in which the inviscid fluxes are obtained with a flux-difference-splitting scheme. At interfaces that delimits the neighboring control volumes, the inviscid fluxes are computed using an approximate Riemann solver based on the values on either side of the interfaces. The Roe flux difference splitting[18] is used in the current study. For second-order accuracy, the interface values are obtained by extrapolation of the control volume centroidal values, based on the gradients computed at the mesh vertices, using an unweighted least squares technique. The Venkatakrishnan[19] limiter is used in the current study to limit the reconstructed values when necessary. In this study, the tetrahedral mesh with prism layers is used. In FUN3D, for tetrahedral meshes, the full viscous fluxes are discretized using a finite-volume formulation in which the required velocity gradients on the dual faces are computed using the Green-Gauss theorem. The solution at each time-step is updated with a backward Euler time-differencing scheme. At each time step, the system of equations is approximately solved with either a multi-color point-implicit procedure or an implicit-line relaxation scheme. Local time-step scaling is employed to accelerate convergence to steady-state. To model turbulent flows, the one-equation model of Spalart-Allmaras[20] (S-A) is used in this study. The volume mesh is shown in Fig.11. The total number of the nodes for the mesh is about 96 million. The volume mesh is comprised of tetrahedral elements and a prism layer near the wall. The prism layer is used to resolve the turbulent boundary layer. The $y+$ of the first cell from the wall is less than 1.

The static aeroelastic simulation module in FUN3D is used for the aeroelastic simulation. The mode shapes are extracted from Boeing NASTRAN model with 50% fuel. Figure 12 shows the first six mode shapes which are interpolated from the NASTRAN mode shapes. The contour color represents the nodal displacement.

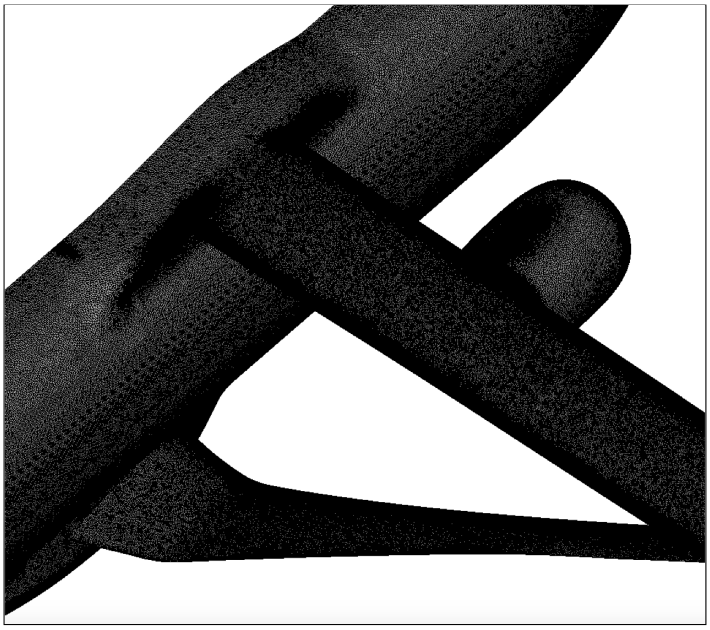

Figure 11 Close View of Mach 0.8 TTBW CFD Mesh

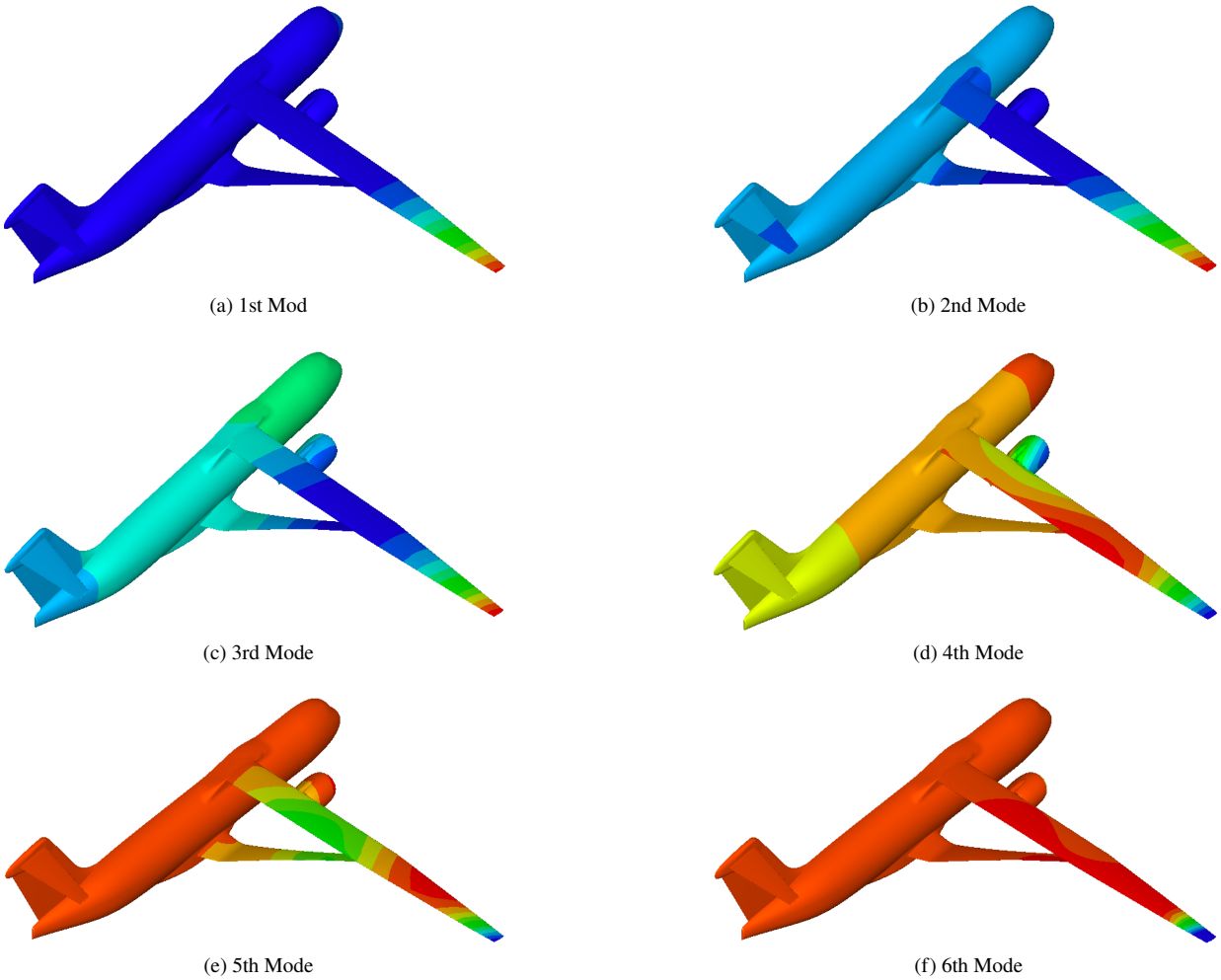

(a) 1st Mod

(b) 2nd Mode

(c) 3rd Mode

(d) 4th Mode

(e) 5th Mode

(f) 6th Mode

Figure 12 Mach 0.8 TTBW Mode Shapes for 50% Fuel.

Deflected control surfaces are created using the process developed in Ref.[10] The various control surfaces undergo rigid body rotations about the hinge line. In this study the gap between the control surfaces are not modeled. In practice these gaps are sealed. A radial basis function smoother applied between control surfaces segments ensures surface continuity between flaps. The surface with the commanded flap rotations is input into the FUN3D code and the volume mesh is deformed. Figure 13 illustrates the high-lift device and control surfaces.

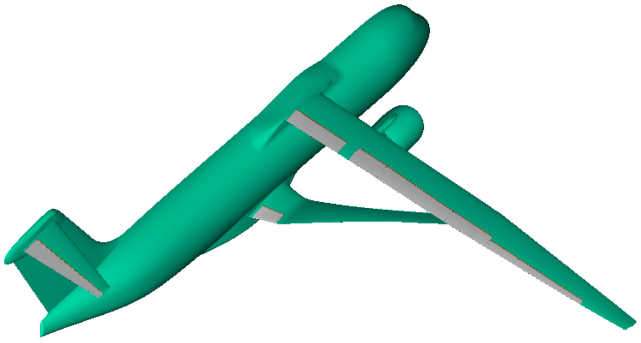

Figure 13 High-lift Devices and Control Surfaces Layout

Figures 14 present the pressure contour comparison of the Jig and design cases at the design $C_{L_2} = 0.695$. The optimized high-lift devices and control surfaces deflections result in a more uniform distribution of the pressure on the aircraft wing surface and thereby helps reduce the drag of the aircraft at the design condition.

Table 11 lists the FUN3D simulation results at the design condition $C_{L_2} = 0.695$. The optimized high-lift devices and control surfaces deflections results in a drag coefficient reduction of 7.2 counts at the design condition as compared to the jig OML geometry. The drag reduction results computed by FUN3D agree well with the VSPAERO results. This confirms the optimization results found by the VSPAERO model.

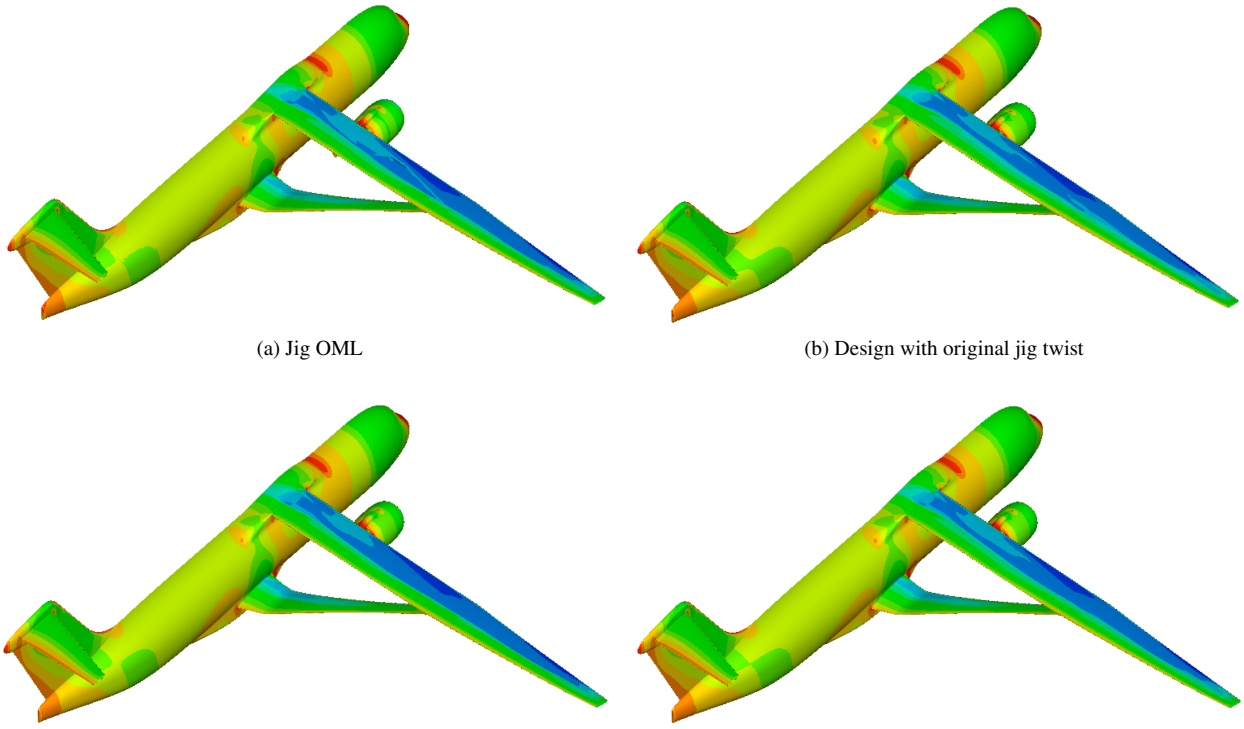

(a) Jig OML

(b) Design with original jig twist

(c) Flight optimized jig twist

(d) Design with optimized jig twist

Figure 14 Pressure Coefficient Contour on the TTBW Geometries at Mach 0.8 and $C_{L_2} = 0.695$

Table 11 Aeroelastic Trim Drag Optimization Results from FUN3D for $C_{L_2} = 0.695$

	C_L	C_D	α (deg)	ΔC_D FUN3D (counts)	ΔC_D VSPAERO (counts)
Jig OML	0.695	0.03273	1.695	-	-
Design (with original jig twist)	0.695	0.03250	1.795	2.3	2.9
Jig twist optimization	0.695	0.03216	1.862	5.7	4.8
Design (with optimized jig twist)	0.695	0.03201	1.958	7.2	6.5

Conclusions

An aeroelastic trim drag optimization study for the Mach 0.8 TTBW aircraft using the high-lift devices and control surfaces is performed based on the in-house developed tool VSPAERO coupled to mode shapes computed by NASTRAN using the Galerkin method for rapid aero-structural analysis. Three flight conditions corresponding to Mach 0.8

and $C_{L_1} = 0.661$, $C_{L_2} = 0.695$, and $C_{L_3} = 0.729$ are used for the aeroelastic trim drag optimization study. The optimization results show a drag reductions of 2.63%, 1.98%, and 2.85% corresponding to $C_{L_1} = 0.661$, $C_{L_2} = 0.695$, and $C_{L_3} = 0.729$, respectively. The high-fidelity CFD solver FUN3D simulation results confirm the aeroelastic trim drag optimization results obtained by the VSPAERO aeroelastic model.

Acknowledgment

The authors wish to acknowledge NASA Advanced Air Transport Technology project for the funding support of this work. The authors also acknowledge Boeing Research and Technology and in particular Christopher Droney, Neal Harrison, Michael Beyar, Eric Dickey, and Anthony Sclafani, along with the NASA technical POC, Gregory Gatlin, for their research conducted under the NASA BAART contracts NNL10AA05B and NNL16AA04B. The research published in this paper is made possible by the technical data and wind tunnel test data furnished under these BAART contracts.

References

[1] Bhatia, M., et. al.. "Structural and Aeroelastic Characteristics of Truss-Braced Wing: A Parametric Study," Journal of Aircraft, Vol 49, No. 1, 2012.

[2] Gundlach, J. F., Tetrault, P. A., Gern, F. H., Nagshineh-Pour, A. H., Ko, A., Schetz, J. A., et. al., "Conceptual Design Studies of a Strut-Braced Wing Transonic Transport," Journal of Aircraft, Vol. 37, No. 6, 2000.

[3] Gur, O., Bhatia, M., Schetz, J.A., Mason, W. H., Kapania, R. K., and Mavris, D. N., "Design Optimization of a Truss-Braced Wing Transonic Transport Aircraft," Journal of Aircraft, Vol. 47, No. 6, 2010.

[4] Harrison, N. A., Beyar, M. D., Dickey, E. D., Hoffman, K., Gatlin, G.M. and Viken, S. A., "Development of an Efficient Mach=0.80 Transonic Truss-Braced Wing Aircraft," AIAA SciTech Conference, AIAA-2020-0011, January 2020.

[5] Nguyen, N., "Elastically Shaped Future Air Vehicle Concept, " NASA Innovation Fund Award 2010 Report, October 2010, Submitted to NASA Innovative Partnerships Program,

[6] Nguyen, N. and Urnes, J., "Aeroelastic Modeling of Elastically Shaped Aircraft Concept via Wing Shaping Control for Drag Reduction," AIAA Atmospheric Flight Mechanics Conference, AIAA-2012-4642, August 2012.

[7] Nguyen, N., Livne, E., Precup, N., Urnes, J., Nelson, C., Ting, E. and Lebofsky, S., "Experimental Investigation of a Flexible Wing with a Variable Camber Continuous Trailing Edge Flap Design, " AIAA 2014-2441, June. 2014

[8] Lebofsky, S., Ting, E., Trinh, K. V., Nguyen, N. T., "Optimization for Load Alleviation of Truss-Braced Wing Aircraft With Variable Camber Continuous Trailing Edge Flap," 33rd AIAA Applied Aerodynamics Confererence, AIAA-2015-2723, June 2015.

[9] Ting, E., Chaparro D., Nguyen, N. T., Fujiwara, G. E., "Optimization of Variable-Camber Continuous Trailing-Edge Flap Configuration for Drag Reduction," Journal of Aircraft, Vol. 55, No. 6, pp. 2217-2239, 2018.

[10] Bartels, R. E., Stanford B. K., Waite, J. M., "Performance Enhancement of the Flexible Transonic Truss-Braced Wing Aircraft Using Variable-Camber Continuous Trailing-Edge Flaps," AIAA 2019-0316, June 17-21, 2019, Dallas, Texas

[11] Xiong, J., Nguyen, N., and Bartels, R. E., "Aerodynamic Optimization of Mach 0.8 Transonic Truss-BracedWing Aircraft using Variable Camber Continuous Trailing Edge Flap," AIAA Science and Technology Forum and Exposition, AIAA-2022-0016, Jan. 2022.

[12] Struber, H., "The Aerodynamic Design of the A350 XWB-900 High Lift System," 29th ICAS, Sep. 2014.

[13] Litherland B. and Rieth K., "VSP Aircraft Analysis User Manual,", July. 2014

[14] Xiong, J., Nguyen, N., and Fugate, J., "Study of Mach 0.8 Transonic Truss-Braced Wing Aircraft Wing- Strut Interference Effects," AIAA Science and Technology Forum and Exposition, AIAA-2021-0336, Jan. 2021.

[15] Xiong, J., Nguyen, N., and Bartels, R. E., "Jig Twist Optimization of Mach 0.8 Transonic Truss-Braced Wing Aircraft, " AIAA Science and Technology Forum and Exposition, AIAA-2023, Jan. 2023.

[16] Biedron, R. T., et al., "FUN3D Manual 13.2,", NASA TM-2017-219661, Aug. 2017

[17] Lee-Rausch, E. M., Hammond, D. P., Nielsen, E. J., Pirzadeh, S. Z., and Rumsey, C. L., "Application of the FUN3D Unstructured-Grid Navier-Stokes Solver to the 4th AIAA Drag Prediction Workshop cases," AIAA Aviation Conference, AIAA-2010-4511, January 2019.

[18] Roe, P. L., "Approximate Riemann Solvers, Parameter Vectors and Difference Schemes,", Journal of Computational Physics, Vol. 46, No. 2, 1980, pp. 357-378

[19] Venkatakrishnan, V., "Convergence to Steady State Solutions of the Euler Equations on Unstructured Grids with Limiters,", Journal of Computational Physics, Vol. 118, No. 1, 1995, pp. 120-130

[20] Spalart, P. R. and Allmaras, S. R., "A One-Equation Turbulence Model for Aerodynamic Flows," AIAA Science and Technology Forum and Exposition, AIAA-1992-0439, January 1992.